High Entropy Alloys & Materials (2024) 2:258–276
https://doi.org/10.1007/s44210-024-00039-x

ORIGINAL PAPER

Characterisation of Phase Separation in Drop-Tube-Processed Rapidly Solidified $CoCrCuFeNi_{0.8}$ High-Entropy Alloy

L. S. E. Teggin[1] · R. F. Cochrane[1] · A. M. Mullis[1]

Received: 3 November 2023 / Accepted: 15 May 2024 / Published online: 6 June 2024
© The Author(s) 2024

Abstract

We investigate the impact of cooling rate on a $CoCrCuFeNi_{0.8}$ high-entropy alloy with a predicted metastable miscibility gap. Rapid solidification via drop-tube processing simulates a containerless, low-gravity solidification environment. Droplets were produced with diameters ranging from 850+ µm to 38 µm, with calculated liquid phase cooling rates of between 600 and 60,000 K s^{-1}. Contrary to studies on similar alloys with a reported metastable miscibility gap and similar investigations on binary alloys known to undergo metastable liquid phase separation, almost no core–shell microstructures were observed in the droplets, likely due to a heavily unbalanced volume fraction ratio between the two phases formed from the parent liquid. Instead, drop-tube processing yielded myriad structures, the occurrences of which vary heavily with cooling rate. At cooling rates of 600 K s^{-1}, a solid-state decomposition reaction begins to become noticeable, populating dendrites with copper-rich dispersions after solidification. The prevalence of these structures increases with increasing cooling rate, occurring in above 95% of droplets once cooling rate exceeds 20,000 K s^{-1}. Occurrence rate of dispersions attributed to liquid phase separation peaks at 8% of droplets at intermediate cooling rates between 5000 and 12,000 K s^{-1}. Spontaneous grain refinement has a maximum prevalence between 1000 and 5000 K s^{-1}. This study begins to show how cooling rate and undercooling can be used to tailor microstructures in HEAs and highlights drastic differences in obtainable microstructures compared to those found in binary and ternary immiscible alloys.

Keywords Rapid solidification · High-entropy alloy · Solid-state decomposition · Liquid phase separation · Grain refinement

Introduction

Rapid solidification of crystalline materials is generally defined as the use of high cooling rate or deep undercooling of a melt to increase the rate of crystallisation [1]. Such deep undercooling can yield microstructures otherwise inaccessible by conventional near-equilibrium solidification. Morphologically, increasing departure from equilibrium tends to yield a continuous refinement of microstructural features [2, 3]. However, above a specified undercooling, spontaneous grain refinement has also been observed, whereby grain size decreases suddenly by up to an order of magnitude [4, 5]. In some cases, rapid cooling causes retention of phases in their metastable state down to room temperature, or the formation of new phases not predicted by the equilibrium phase diagram [6, 7]. Extended solid solubility can be observed when solidifying far from equilibrium [8] and solute trapping can occur when the velocity of the solidification front approaches the speed of diffusion of solute across the solid–liquid interface [9]. Moreover, in some cases, full partitionless solidification can be achieved, where the solidified structure has the same composition as the liquid from which it grows [10, 11]. Often, a combination of these effects is responsible for changes in mechanical properties brought about by rapid solidification such as martensitic transformations in quenched steels and titanium alloys [12] or the suppression of soft FCC phases in favour of harder BCC phases [13]. In high-entropy alloys, $Al_xCoCrFeNi$ alloys gain strength during rapid cooling due to microstructural refinement and retainment of stronger BCC phases down to room temperature [14, 15]. However, a similar effect is not observed when refining lamellar spacing in eutectic $AlCoCrFeNi_{2.1}$, where retention of a softer FCC phase

✉ L. S. E. Teggin
pm15lset@leeds.ac.uk

[1] School of Chemical and Process Engineering, University of Leeds, Leeds LS2 9JT, UK

counteracts any strengthening structural refinement would cause [16].

In alloys with a positive enthalpy of mixing and a miscibility gap in the phase diagram, liquid phase separation (LPS) can occur. On cooling, the parent liquid L separates into two liquids with differing compositions, L_1 and L_2, to minimise free energy. Here, L_2 refers to the phase occupying the minority volume fraction. In the case of binodal LPS, the L_2 phase will initially nucleate in the form of minority phase droplets (MPD) in the parent liquid, which can then grow, move throughout the melt, and possibly coalesce into various microstructures. The most useful LPS behaviour, occurring in the metastable regime (where critical temperature for LPS initiation falls below the liquidus), is still sparsely treated [17, 18]. The first alloys shown to exhibit this behaviour were Co–Cu and Cu–Fe, investigated by Nakagawa et al. [19]. Since then, immiscible alloys have been studied based on their potential to form valuable composite materials. The most sought after obtainable structures are core–shell structures (where a core of one phase migrates to the centre of the droplet under the action of Marangoni convection to be surrounded by a shell of the other phase), and finely dispersed structures [17]. Core–shell structures have found potential application in electronic packaging, where the core of a highly electrically conductive phase can be surrounded by the shell of an easily melting solder. This possibility has been explored in systems such as Al–Bi–Sn [20–22]. Fine dispersions, for example, of a soft phase in a harder phase, yield a combination of properties useful in machine bearings. The soft phase allows debris to embed and reduce damage to other components while the hard phase maintains structural integrity under load [23].

Jegede et al. [24] investigated the impact of rapid solidification in a drop-tube on metastable Co–Cu binary alloys. They found that dendritic structures prevailed at lower cooling rates (larger droplets), where critical undercooling is less likely to be achieved. Incidence of core–shell structures peaked at intermediate cooling rates. At the highest cooling rates, finely dispersed structures became more prevalent. Intermediate cooling rates are thought to provide the perfect conditions for core–shell formation, where cooling rate is sufficiently rapid to provide the undercooling required for nucleation of the L_2 phase, but the time between nucleation and solidification remains sufficient to allow significant Ostwald ripening and coalescence through movement of the L_2 phase MPDs via Marangoni convection. This sequence of transformations was echoed in a study of drop-tube-processed ternary Al–Sn–Cu alloys by Yan et al. [25].

Among HEAs exhibiting exclusively solid solution phases upon solidification, the CoCrCuFeNi compositional family of alloys is the only extensively studied alloy group known to undergo LPS in the metastable regime [18]. At near-equilibrium conditions, equiatomic CoCrCuFeNi solidifies dendritically to a copper-rich and copper-lean phase [26]. However, it has been shown that the alloy exhibits behaviour associated with metastable LPS upon undercooling in a similar fashion to binary alloys. High undercooling experiments on $CoCrCu_xFe_yNi_z$ alloys also suggest that composition affects the critical undercooling required to initiate LPS. Liu et al. [27] studied $CoCrCuFe_xNi$ alloys, where $x = 1$, 1.5 and 2 via flux undercooling. Metastable LPS occurred in all alloys studied, with critical undercooling increasing with increasing iron content. The authors observe copper-rich spheres embedded in a copper-lean matrix, with an "egg-type" microstructure forming at higher undercoolings, this presumably constitutes a core–shell structure, where a denser core has migrated to the bottom of the sample under the effect of gravity. Conversely, Wu et al. [28] found that $CoCrCuFe_{0.5}Ni$ and $CoCrCuFeNi_{0.5}$ undergo stable LPS. Wang et al. [29] glass fluxed the equiatomic alloy and achieved LPS at 223 K. The single-phase liquid separated into an FCC high-entropy phase and a copper-rich phase, which occupied a minor but increasing volume fraction of the final microstructure as undercooling was increased. Guo et al. [30], after glass fluxing the equiatomic alloy, determined a much lower critical undercooling of 100 K. Like Liu et al. initial LPS of the minor phase on a small scale gives way to noticeable "egg-type" microstructures at higher undercoolings. $CoCrCu_xFeNi$ alloys were glass fluxed by Wang and Kong [31], with metastable LPS initiated at a critical undercooling of 180 K. LPS in the interdendritic regions of the alloy at lower undercoolings gives way to copper-rich globules present at the bottom of the sample with increasing undercooling. A full layer of copper-rich phase forms at the bottom of the sample at the highest undercoolings, which is attributed to Stokes motion. The lowest undercooling required for LPS in these alloys was achieved by Lin et al. [32] who observed a core–shell structure after undercooling $CoCrCuFe_{1.5}Ni_{0.5}$ alloy by 43 K through glass fluxing. A summary of studies involving critical undercooling required for LPS in variations of $CoCrCu_xFe_yNi_z$ is shown in Table 1.

Given the useful structures achievable when initiating LPS in binary and ternary alloys, as well as the notable materials properties potentially obtainable through exploration of HEAs, we believe it is promising to study the response of immiscible HEAs to a rapid solidification environment. It is also important to compare this behaviour to established research on more compositionally simple immiscible alloys. To study LPS, we use drop-tube processing to subject alloys to rapid solidification, achieve high undercooling and simulate a low-gravity environment [17].

The aims of this study are as follows:

1. Catalogue and investigate the microstructures achievable during rapid solidification of a high-entropy alloy with a metastable miscibility gap

Table 1 Liquid phase separation behaviour of $CoCrCu_xFe_yNi_z$ alloys

Alloy	Critical undercooling/K	Cooling method	Study
CoCrCuFeNi	100	Glass fluxing	[30]
	160	Glass fluxing	[27]
	223	Glass fluxing	[29]
	180	Glass fluxing	[31]
	No LPS	Crucible casting	[33]
$CoCrCuFeNi_{0.5}$	Stable LPS	Crucible casting	[33]
$CoCrCuFe_{0.5}Ni$	Stable LPS	Crucible casting	[33]
$CoCrCuFe_{1.5}Ni$	190	Glass fluxing	[27]
$CoCrCuFe_2Ni$	293	Glass fluxing	[27]
$CoCrCu_2FeNi$	217	Glass fluxing	[31]
$CoCrCuFe_{1.5}Ni_{0.5}$	43	Glass fluxing	[32]

2. Compare the phase formation behaviour in drop-tube-processed HEAs to similar binary alloys with a metastable miscibility gap in their phase diagrams

To our knowledge, no previous studies of the CoCrCuFeNi system have been conducted where the alloy has been solidified via drop-tube processing. Within the CoCrCuFeNi composition space, we select an alloy for study with the goal of increasing the likelihood of LPS. From the equiatomic alloy, CoCrCuFeNi, we have lowered nickel content to form $CoCrCuFeNi_{0.8}$. Data from Table 1 show that $CoCrCuFeNi_{0.5}$ liquid phase separates in the stable regime, without need for undercooling. Conversely, the equiatomic alloy exhibits LPS in the metastable regime with an average required undercooling of 165 K. Nickel addition has also been shown to raise critical undercooling in other high-entropy alloys [18, 34]. Therefore, it is hypothesised that, at a composition of $CoCrCuFeNi_z$ where $0.5 < z < 1$, critical undercooling will be lower than the equiatomic alloy, but not so low as to induce stable LPS.

Experimental Method

Pure cobalt, chromium, copper, iron and nickel, of purity > 99%, were arc melted together in the correct ratio to form a master alloy of $CoCrCuFeNi_{0.8}$. Each alloy formed as part of this process (CoFe, $CuNi_{0.8}$, $CoCuFeNi_{0.8}$ and $CoCrCuFeNi_{0.8}$) was remelted at least three times to ensure full mixing. An 8.1 g sample of the alloy was drop-tube processed. Drop-tube processing entails pressurised ejection of liquid alloy through small orifices to form a large number of droplets of varying sizes. These droplets solidify in freefall through a tube containing a low-pressure inert gas atmosphere. Specific experimental details regarding use of the drop-tube apparatus at the University of Leeds can be found in [13]. The resultant solidified droplets were collected and sieved into nine size fractions: 850+, 850–500, 500–300, 300–212, 212–150, 150–106, 106–75, 75–53 and 53–38 µm. The $CoCrCuFeNi_{0.8}$ ingot and powders from each size fraction were cold-mounted separately in resin. The samples were ground with P400 and P1200 SiC paper and subsequently with 3 µm and 1 µm diamond paste polish. 0.05 µm colloidal silica was used as the final polishing step.

A Carl Zeiss LSM800 Mat CLSM confocal microscope with automatic montage facility was used to collect qualitative structural data on samples. A laser acts as the microscope light source allowing greater resolution than a conventional optical microscope of similar aperture, thereby allowing sufficient delineation between structures for classification. Multiple photographs, each consisting of four stitched tiles, were taken at varying locations across the sample, with no overlap allowed between photographs to avoid counting the same droplet(s) twice. Photographs were taken in this manner until a sufficient number was available from which to view, analyse and classify at least 250 droplets. Over 500 droplets were counted for the 75–53 µm size fraction to conduct a deeper statistical analysis, which is detailed in Appendix 1. We demonstrate that a sample size of $n \geq 250$ is sufficient to ensure the sample is descriptive of the whole droplet population within a given sieve fraction. We also discuss an approach to uncertainty quantification for the occurrence of each treated structure to determine the statistical significance of observed trends.

Detailed analysis of microstructures was undertaken using a Hitachi SU8230 SEM. Composition data were obtained using the attached EDX apparatus on the SEM. The melting point of the ingot sample was determined through DSC analysis.

A fully experimental measurement of cooling rate during drop-tube processing is not possible for small droplets in flight. Instead, we utilise a theoretical model of heat flux over spherical droplets of different sizes when in free fall through an atmosphere. The heat balance is treated in [13, 24, 35] and, for the sake of brevity, is not repeated here.

Analysis of relative volume fraction of phases was undertaken using binarisation of relevant SEM micrographs with ImageJ® software.

Results

Composition in the Ingot and Droplets

Atomic percentages of each constituent element in the arc-melted ingot sample and the drop-tube-processed 75–53 µm droplets are shown in Table 2 based on EDX analysis.

Composition values alter the element ratios slightly but are largely in the required range for use in this study.

Table 2 Atomic percentage of constituent elements in arc-melted and drop-tube-processed (75–53 μm) $CoCrCuFeNi_{0.8}$

	Co/at.%	Cr/at.%	Cu/at.%	Fe/at.%	Ni/at.%
Ingot	20.72 ± 0.08	22.12 ± 0.03	20.70 ± 0.18	20.43 ± 0.06	16.03 ± 0.06
75–53 μm droplets	20.56 ± 0.02	21.74 ± 0.07	20.55 ± 0.04	20.87 ± 0.06	16.29 ± 0.03

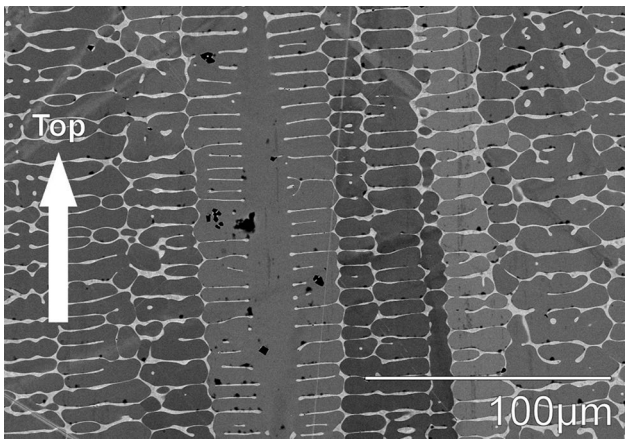

Fig. 1 SEM micrograph of $CoCrCuFeNi_{0.8}$ regular dendrites near dome top. The darker phase is CoCrFeNi-rich while the lighter minority phase is Cu-rich

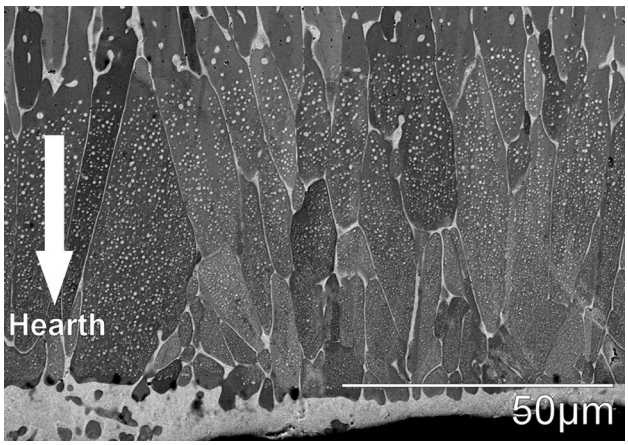

Fig. 2 SEM micrograph of $CoCrCuFeNi_{0.8}$ dispersions and macrosegregation near copper hearth. The darker phase is CoCrFeNi-rich while the lighter minority phase is Cu-rich

Therefore, from this point forward, we use $CoCrCuFeNi_{0.8}$ to nominally describe the composition of the alloy on which this work is based.

Arc-Melted $CoCrCuFeNi_{0.8}$

The sectioned arc-melted ingot is largely composed of a CoCrFeNi-rich high-entropy (HEA) phase and a copper-rich phase that occupies a much lower volume fraction. The two-phase morphology in the bulk of the ingot microstructure is consistent with past work on the equiatomic alloy and other compositional variants, wherein both phases have been confirmed to have a FCC structure. Morphology changes from purely dendritic at the top of the ingot (furthest from the copper hearth and encountering the lowest cooling rate) to a dispersion of the copper-rich phase in the high-entropy phase closer to the hearth (Figs. 1 and 2, respectively). Finally, a large deposit of copper-rich phase is observed in the ingot closest to the hearth (the area with the highest cooling rate). We assume this consolidation of copper-rich phase near the hearth is due to gravity-aided macrosegregation, where the denser copper-rich liquid migrates to the bottom of the sample after separation. The composition of the dendritic (D) and interdendritic (IDP) phases does not change extensively across the sample. This is shown in Table 3.

The copper-rich interdendritic phase contains between 81 and 84 at.% copper, with the remaining four elements making up the difference. Of the minority elements, chromium is present in the lowest quantity (between 2 and 4 at.%), while nickel is the most prevalent (at around 6–7 at.%). In the dendritic HEA phase, the copper that has not partitioned to the interdendritic phase makes up about 10 at%. The percentage of nickel at between 16 and 17 at% reflects the reduction in nickel content compared to the equiatomic. Iron, chromium and cobalt are present in quantities exceeding 20 at.%.

Drop-Tube-Processed $CoCrCuFeNi_{0.8}$

Drop-tube processing yielded powders from all size fractions apart from the < 38 μm size fraction, where not enough powder was gathered for analysis.

Cooling Rate Determination

Figure 3 shows that droplet liquid phase cooling rate dT_d/dt varies with droplet size d following a power-law relationship $dT_d/dt = 1.3 \times 10^7 d^{-1.44}$. Average cooling rates vary between 600 K s^{-1} for the largest droplets and 60,000 K s^{-1} for the smallest with even higher maximum cooling rates possible with the smallest droplets in the 53–38 μm size fraction. Thermophysical properties for $CoCrCuFeNi_{0.8}$ were either estimated based on the mixture rule or gathered experimentally using DSC analysis in the case of the alloy

Table 3 Normalised EDX-derived compositions for dendritic and interdendritic phases in varying parts of the arc-melted $CoCrCuFeNi_{0.8}$ ingot

Location (phase)	Co/at.%	Cr/at.%	Cu/at.%	Fe/at.%	Ni/at.%
Hearth (D)	24.19 ± 0.32	25.05 ± 0.17	9.97 ± 0.25	23.93 ± 0.21	16.85 ± 0.38
Hearth (IDP)	4.11 ± 0.97	4.31 ± 1.66	81.29 ± 4.92	4.17 ± 1.31	6.12 ± 1.32
Centre (D)	25.54 ± 0.21	25.40 ± 0.16	9.79 ± 0.22	23.95 ± 0.30	16.32 ± 0.35
Centre (IDP)	3.26 ± 0.12	2.71 ± 0.17	83.83 ± 0.73	3.27 ± 0.20	6.93 ± 0.35
Top (D)	24.40 ± 0.64	25.15 ± 0.19	9.79 ± 0.11	24.06 ± 0.23	16.61 ± 0.94
Top (IDP)	3.30 ± 0.34	2.92 ± 0.49	83.20 ± 2.25	3.39 ± 0.52	7.19 ± 1.36

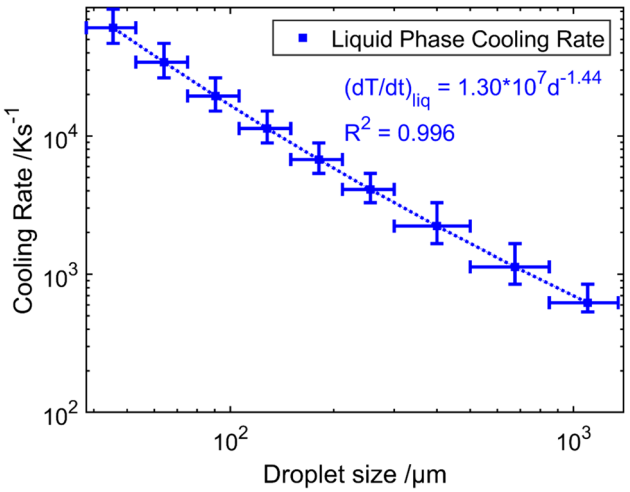

Fig. 3 Theoretical cooling rate variation with droplet diameter in drop-tube-processed $CoCrCuFeNi_{0.8}$ alloy

melting point. The thermophysical properties of each constituent element were determined using data from [36–38]. The output of the DSC analysis (Online Resource 1) and a summary of data used to determine cooling rate from droplet size (Online Resource 2) are both available in the supplementary information.

Structural Classification and Analysis

In similar studies involving rapid solidification-induced LPS in binary alloys, the categorisation is not binary, even when searching for the presence of a single structure such as core–shell. Rather, authors often note a wide range of structures including evolving core–shell structures and multi-layer core–shell structures. This is not to mention dendritic structures and fine dispersions, which also occur in various configurations [24]. A wide range of structural occurrence is what we also, predictably, find in this work. Findings in this experiment include single- and multi-crystalline dendritic droplets, droplets in various stages of grain refinement and dispersions occurring in large scales within droplets or localised within dendrite arms. A classification system was developed to better differentiate repeatedly occurring structures and their relative frequency of occurrence in each size fraction. During tallying, a total of 18 categories was used, but for simplicity, these are then amalgamated into five broad categories as follows:

1. Regular dendritic—including single-crystal (SC) and multi-crystal (MC) structures.
2. Dendrite dispersions—dendritic structures featuring dispersions within dendrite arms or within refined grains. This includes single-crystal (SCDD) multi-crystal (MCDD) dendritic structures, partially (PGRDD and PGRDD + Cell) and fully (FGRDD and FGRDD + Cell) grain-refined structures and also includes rarer structures such as extra fine (ExFDD) and highly globular (HGDD) dendrites with dispersions present.
3. Large dispersions—including large dispersions not attributed to dendrite arms or the centres of refined grains. This includes large dispersions present at the droplet periphery which are either cellular (CDOP) or continuous (LDOP).
4. Grain-refined structures—including partially (PGR) or fully (FGR) grain-refined structures without dispersions, including those with cell-like structures (FGR + Cell and PGR + Cell, respectively) as well as partially (PGRDD and PGRDD + Cell) or fully (FGRDD and FGRDD + Cell) grain-refined structures (with and without a cellular structure) featuring dispersions in the refined grains.
5. Rare structures—including any structures not covered by the previous categories, including conventional liquid phase separation structures such as core–shell (CS) and evolving core–shell (ECS) structures.

Given that there are many instances of droplets featuring a microstructure including more than one of these categories (a droplet may be partially grain refined, for example, and still feature dispersions in the fragmented dendrites), these categories feature a substantial amount of overlap. However, accounting for this overlap allows the true extent of occurrence of a certain structure to be better catalogued as we decrease droplet size. Examples of droplets displaying these structures are shown in Fig. 4.

Figure 4a and b show examples of category 1 single- and multi-crystal dendritic structures. Figures 4c and d show

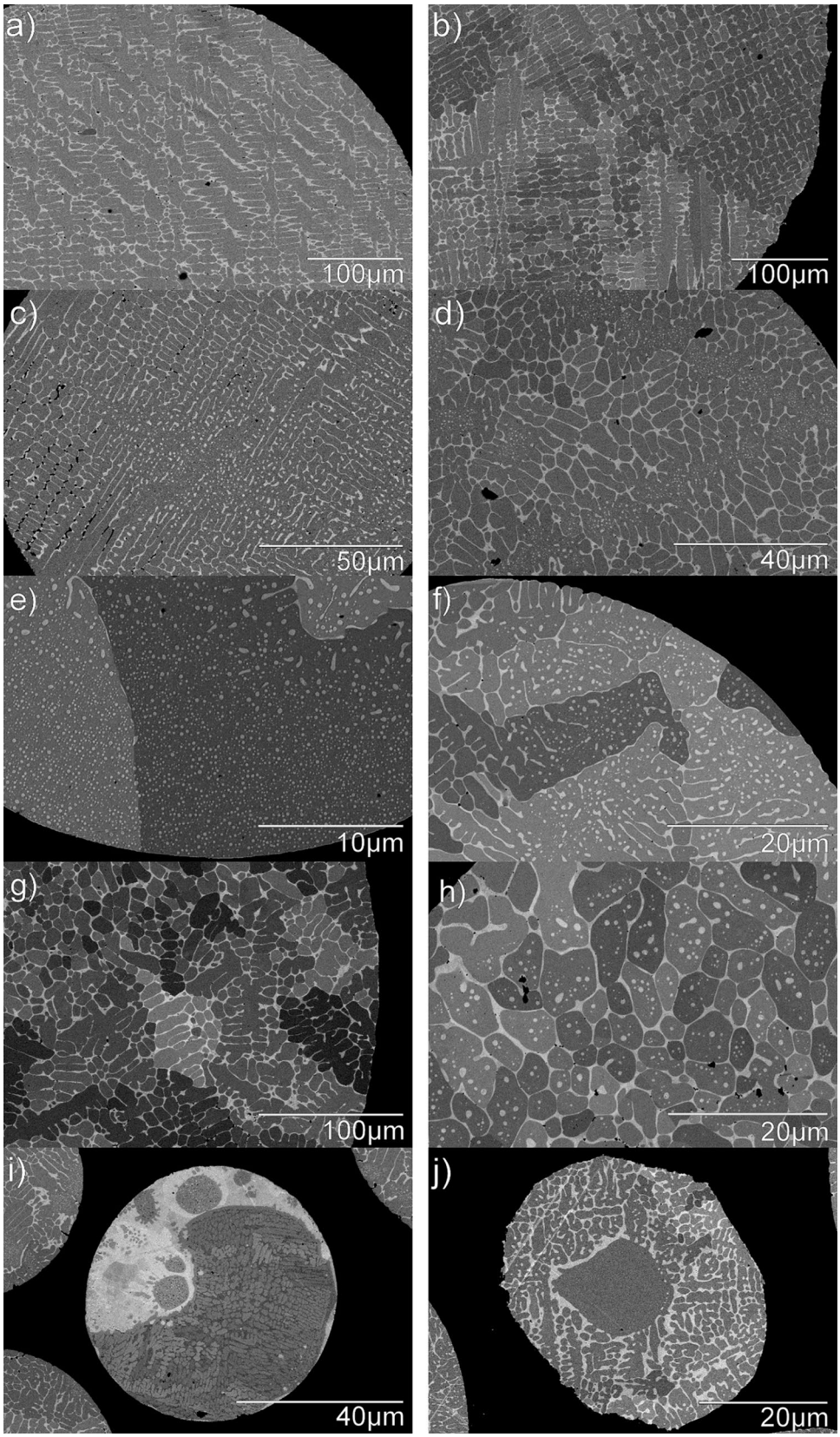

Fig. 4 SEM backscattered images showing examples of categorised microstructures discovered in drop-tube-processed $CoCrCuFeNi_{0.8}$. In all micrographs, the darker phase is CoCrFeNi-rich while the lighter minority phase is Cu-rich. **a, b** Category 1—single and multi-crystal dendritic structures with no dendrite dispersions. **c, d** Category 2—examples of dispersions that may be present in dendritic, partially grain-refined and fully grain-refined microstructures. **e, f** Category 3—large continuous and cellular dispersions of the copper-rich phase in the copper-lean phase. **g, h** Category 4—examples of partially and fully grain-refined structures with or without dispersions in the refined grains. **i, j** Category 5—rare conventional liquid phase separation structures including evolving and fully formed core–shell structures, respectively

examples of category 2 dispersions within dendrite arms. These can be present to a lesser (Fig. 4c) or greater (Fig. 4d) extent throughout the droplet microstructure. Figures 4e and f show examples of category 3 large continuous (LDOP) and cellular (CDOP) dispersions. These are distinct from category 2 dispersion-based structures as these large dispersions are not confined to dendrite arms. Figure 4g and h show droplets in category 4 in different stages of grain refinement (partial and full, respectively). As shown in Fig. 4h, dispersions can also be present within the refined grains. Figure 4i and j show some examples of unusual, rare category 5 structures including partially and fully formed core–shell structures. Further specific examples of category 2 structures with fine dispersoids present in dendrite trunks are shown in Figs. 5, 6 and 7. Figure 5 displays the extent to which dispersoids can be present within primary, secondary and tertiary dendrite trunks. Figures 6 and 7 compare the relative size of dendrite dispersoids across larger and smaller droplet sizes, respectively.

In this study, we focus primarily on the prevalence of categories 2, 3 and 4 that isdendritic dispersions, large dispersions and grain-refined structures, respectively. Droplets including satellites (one droplet colliding with another) were removed from the overall statistical analysis given that these impacts do not represent the containerless solidification being studied. Because a slightly different number of total droplets were counted in each size fraction during the classification, we divide the number of each structure present by the total droplets analysed in the relevant size fraction to yield a percentage value for better comparison across size fractions. The percentage occurrence of structures in categories 2, 3 and 4 across different droplet sizes and cooling rates is shown in Figs. 8, 9 and 10, respectively.

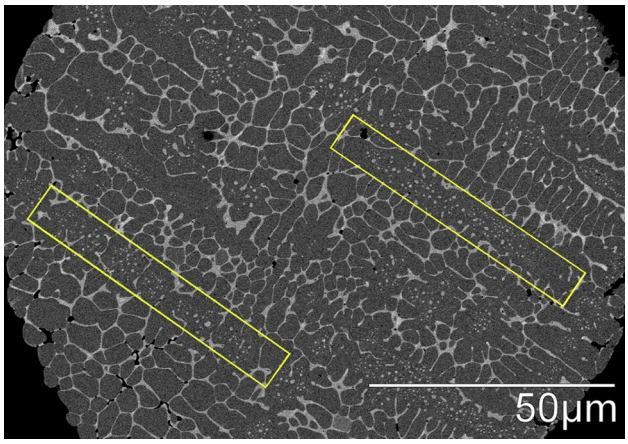

Fig. 6 Dendritic dispersions (category 2) in the 212–150 µm size fraction of drop-tube-processed $CoCrCuFeNi_{0.8}$ particles. Some of the regions featuring dispersions in the dendrite arms are defined by the yellow rectangles. The darker phase is CoCrFeNi-rich while the lighter minority phase is Cu-rich

Structural Trend Analysis—Dispersions in Dendrite Arms

Figure 8 shows that at large droplet sizes, there are very few droplets which display solid-state dispersions of the copper-rich phase within the dendrite arms. Their prevalence increases as droplet size decreases (and cooling rate increases) until the point where, in the smallest size fractions, nearly all analysed droplets display dispersions in the dendrite arms, provided there are dendrites present in the microstructure, whether they have undergone grain refinement or not. Uncertainty in the percentage occurrence of these dispersions is the low due to the ease of identification of the presence or absence of these structures compared to large dispersions and grain refinement.

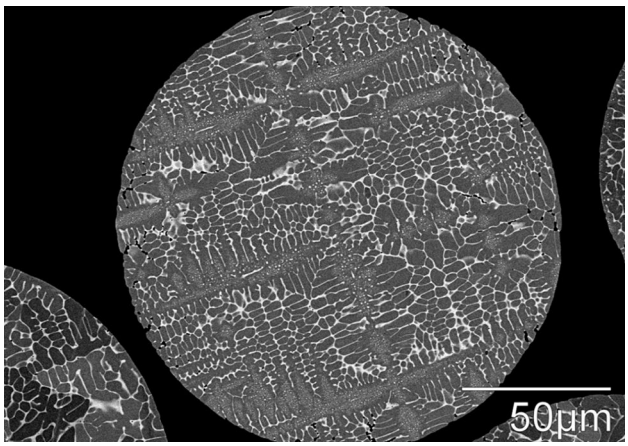

Fig. 5 Extent of copper-rich dendritic dispersions (category 2) present in solidified $CoCrCuFeNi_{0.8}$ droplets. The darker phase is CoCrFeNi-rich while the lighter minority phase is Cu-rich

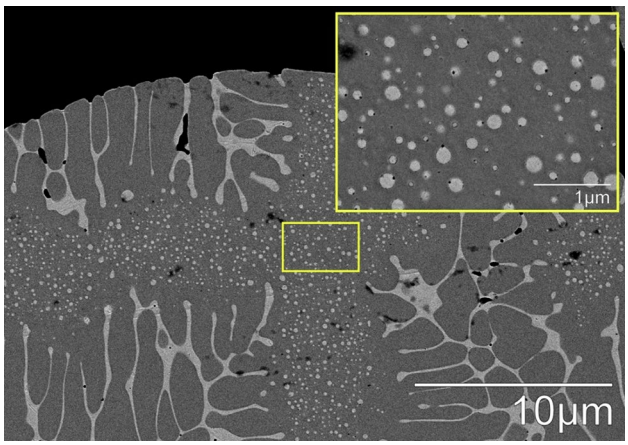

Fig. 7 Dendritic dispersions (category 2) in the 53–38 µm size fraction of drop-tube-processed $CoCrCuFeNi_{0.8}$. The darker phase is CoCrFeNi-rich while the lighter minority phase is Cu-rich

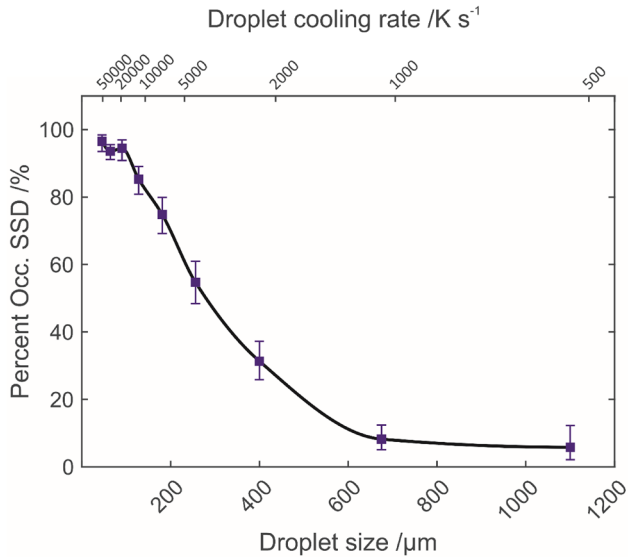

Fig. 8 Percentage occurrence of solid-state dispersions (SSD) as a function of droplet size and cooling rate in drop-tube-processed $CoCrCuFeNi_{0.8}$

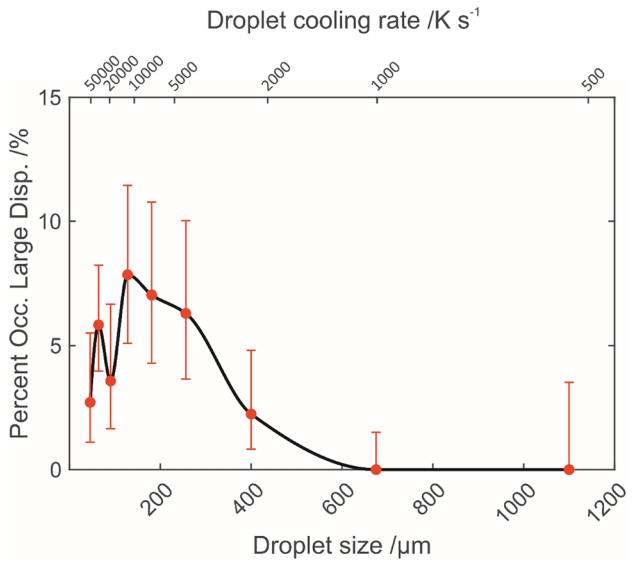

Fig. 9 Percentage occurrence of large dispersion structures as a function of droplet size and cooling rate in drop-tube-processed $CoCrCuFeNi_{0.8}$

These dispersions are overwhelmingly located in primary dendrite arms, but may occasionally be found in secondary and tertiary arms as well. For example, the presence of solid-state dispersions in primary, secondary and tertiary arms is easily recognisable in droplet in Fig. 5. However, only the primary arms are populated in the droplets in Figs. 6 and 7.

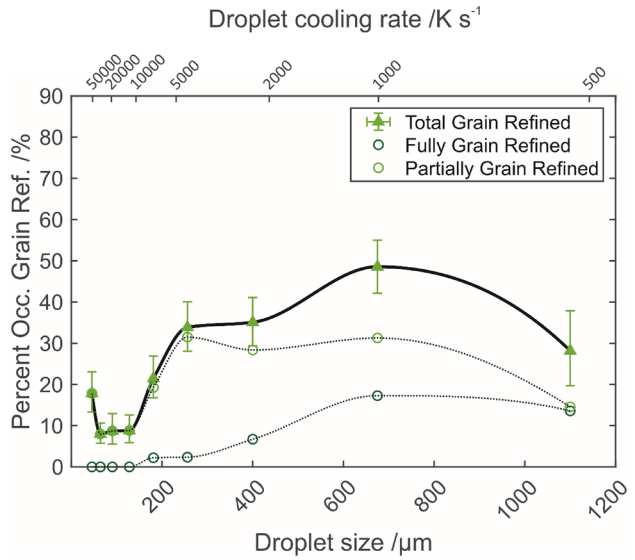

Fig. 10 Percentage occurrence of Grain Refinement (Grain Ref.) as a function of droplet size and cooling rate in drop-tube-processed $CoCrCuFeNi_{0.8}$

Structural Trend Analysis—Large Dispersions

Figure 9 shows that large dispersion structures, where dispersions make up a large proportion of the droplet and are not able to be linked to the arms of specific dendrites, only ever make up a maximum of about 8% of droplets in any given size fraction. Trends found in the percentage occurrence of these structures in the droplets are therefore more uncertain, but still worth discussing. Large dispersions are most common at intermediate droplet sizes of 300–150 μm and corresponding cooling rates of 5000–12,000 K s^{-1}. Given the high uncertainty in these results, we cannot rule out that the decrease in occurrence in the 106–75 μm size fraction is an artefact, and that a single maximum of occurrence rate of these dispersions exists at intermediate cooling rates. Within all individual droplet size fractions, the majority of these large dispersions are continuous (LDOP), with cellular variants (CDOP) making up the remaining minority. In addition, the prevalence of both types of large dispersions appears to increase and decrease in a similar fashion as droplet size is decreased and cooling rate increased.

Given the large dispersions occur seemingly independent of solidifying dendrites (as opposed to the dispersoids in the dendrite arms), they were likely formed before dendrite formation, i.e. when the droplet was in the liquid state. This, and the globular and/or spherical morphology of the dispersoids, means we therefore attribute these large dispersion structures to liquid phase separation in the droplet. The copper-rich phase is therefore the L_2 minority phase in the scenario, with the CoCrFeNi-rich phase being the L_1 phase. Any LPS which occurs seems to result in fine dispersions

of copper-rich MPDs or globules in drop-tube solidified $CoCrCuFeNi_{0.8}$.

Structural Trend Analysis—Spontaneous Grain Refinement

From Fig. 10, we see that incidence of grain refinement (partial or full) peaks at about 50% in droplets with diameters of between 600 and 800 µm and cooling rates of below 5000 K s^{-1}. This value dips to a low of below 10% at the second smallest size fraction of 75–53 µm before a small but statistically significant rise in the smallest size fraction of 53–38 µm. This is a notable trend as two separate peaks may indicate multiple mechanisms are responsible for grain refinement in the droplets at different prevailing cooling rates, which is consistent with some of the previous literature [4]. Fully grain-refined structures, with a droplet cross section being almost entirely made up of equiaxed grains small compared to droplet diameter, are only observed to occur at lower cooling rates, with their prevalence decreasing from a maximum of nearly 20% at cooling rates of 1000 K s^{-1} to nearly 0% once cooling rates reach just above 10,000 K s^{-1}. Incidence of partial grain refinement, highly prevalent at lower cooling rates of 1000 K s^{-1} also become less common as cooling rates rise above 1000 K s^{-1} with a minimum in smaller droplets subject to cooling rates of 10,000 K s^{-1} to 35,000 K s^{-1}. The noticeable rise in occurrence of partially grain-refined structures at high cooling rates of around 60,000 K s^{-1} in the smallest size fraction is not observed to occur in the incidence of fully grain-refined droplets.

Discussion

General Trends in Phase Composition and Morphology

Possible reasons for the trends in the element partitioning across the phases are well discussed in the previous literature. Derimow and Abbaschian [18] analysed the as-cast microstructures of an extensive array of multiprinciple element alloys based on the additions to the CoCrCu base group. Their results show that on solidification, alloys containing copper usually separate into a copper-rich and copper-lean phase. A copper-rich liquid forms in the event of LPS, while if dendritic solidification occurs, the relatively copper-lean dendrites will typically grow into a copper-rich interdendritic phase. From there, the preferential segregation of elements into the copper-rich or copper-lean phases during solidification seems to depend on the enthalpy of mixing between the introduced species and the other elements already present in the alloy [26, 28, 30–34, 39–44]. Of the alloying elements, nickel possesses the lowest positive enthalpy of mixing with copper [45]. It is understandable, therefore, that nickel forms the largest minority element in the copper-rich interdendritic phase in the arc-melted and drop-tube-processed alloy. However, while nickel mixes well (or rather, the least badly) with copper, it still has a negative enthalpy of mixing with chromium, cobalt and iron, which explains why the bulk of the nickel still occupies the copper-lean dendrites. As another example, chromium, with the most positive enthalpy of mixing with copper of the other four elements, is predictably present in the lowest quantities in the copper-rich phase.

Arc-Melted $CoCrCuFeNi_{0.8}$

Analysis of the alloy ingot sample indicates potential for this alloy to undergo LPS in the metastable regime given the drastic change in structure with increasing cooling rate. The dendritic, two-phase structure present in the regions of the arc-melted button further from the water-cooled copper hearth (Fig. 1) resembles those found in separate studies where equiatomic CoCrCuFeNi was solidified via near-equilibrium solidification methods [26, 46, 47]. This dendritic structure does not, however, occupy the full cross section of the sample. Instead, the fine copper-rich dispersions apparent in the narrow region nearest to the hearth, as well thin layers of fully separated copper-rich phase in this area, suggest that LPS is occurring near the hearth where cooling rate is highest. After LPS, Stokes sedimentation due to gravity would likely cause the denser copper-rich phase to settle at the bottom of the sample and cause the stratification shown in Fig. 2. The composition of the dendritic and interdendritic phase in the arc-melted $CoCrCuFeNi_{0.8}$ is generally similar to that found by Derimow et al. [47] for the equiatomic alloy in terms of the ratio of elements in each of the phases.

Microstructures Formed in Drop-Tube-Processed $CoCrCuFeNi_{0.8}$

Dispersions in Dendrite Arms

Dispersions in dendrite arms first occur at least occasionally in the largest 850+ µm size fraction but are present in above 80% of droplets once droplet diameter drops below around 200 µm. Given that primary dendrite arms are so called because they form first during dendritic solidification, we reassert that the dispersions described in "Structural Trend Analysis—Dispersions in Dendrite Arms" section are a separate phenomenon to the LPS discussed in "Structural Trend Analysis—Large Dispersions" section. It is, to us, impossible to explain how a morphology with such consistent placement of dispersoids in the primary dendrite arms could form without simultaneously accepting that dispersions form preferentially in these areas after the dendrites themselves have formed. We therefore postulate that these

dispersoids are likely the result of decomposition in the solid state.

Thermodynamic instability in HEAs in the solid state is not unheard of. The Cantor alloy, for example, becomes thermodynamically unstable at low-to-intermediate temperatures where prolonged annealing was seen to cause the formation of $L1_0$, B2 and BCC phases at the grain boundaries [48, 49]. However, we believe it quite unusual for micro-scale dendritic dispersions to be formed in primary dendrite arms directly after the initial solidification reaction and which cannot be suppressed by cooling rates up to 60,000 K s^{-1}.

The relatively consistent increase shown in Fig. 8 indicates a strong positive correlation between cooling rate and incidence rate of solid-state dispersions. Because very few droplets with dispersions are found in larger size fractions, we reason that a minimum undercooling is required to cause the HEA solid solution to become sufficiently supersaturated with copper. The supersaturated solid solution then decomposes into copper-rich dispersoids in a copper-lean phase. What causes the supersaturation?

The solidifying dendrites are formed compositionally of the CoCrFeNi-rich (HEA) phase, which has a higher melting point than the copper-rich interdendritic phase, meaning the dendrites nucleate, likely heterogeneously and grow within a copper-rich melt. As the dendrites of the HEA phase grow, they reject solute (in this case, mostly copper) into the remaining liquid, enriching it with copper. Increased prevailing cooling rates will also generally increase the undercooling of the droplet. This will, in turn, increase dendrite growth velocity. In line with the model of solute trapping proposed by Aziz [50], the increase in growth velocity can enhance solute trapping and resultant supersaturation of the growing solid phase. At a critical undercooling, the dendrite growth velocity of the nucleated HEA solid in the liquid will become larger than the speed at which copper solute atoms rejected by the HEA phase can diffuse into the remaining liquid [50], resulting in supersaturation of the HEA phase with copper. Indeed, the presence of copper-rich dispersions within the dendrites seems to confirm that the dendrites were previously supersaturated with copper before such a transformation occurred. We therefore propose that the compositional and thermal gradients present provide adequate driving force for either nucleation of a solid copper-rich phase within the solid HEA dendrites or the crossing of a spinode causing spinodal decomposition in selected areas within the dendrite cores. A diffusion-controlled transformation would then slow and cease once the temperature dropped too low to continue providing the energy needed to facilitate long range substitutional diffusion of copper through the lattice. In the case of spinodal decomposition, coarsening of the dispersoids would also be rendered impossible as temperature decreases. The solid-state dispersions in this alloy, qualitatively, appear to become finer and decrease in size at a similar rate to the dendrites in which they nucleate and thus, the droplets in which they are found. This is likely due to the decrease in time available for coarsening of the copper-rich dispersoids in smaller droplets due to the higher cooling rates to which they are subjected. This trend can be observed by comparing Figs. 6 and 7. Figure 6 shows a droplet in the 212–150 µm, with the largest dendritic dispersions nearing a diameter of 1 µm. Figure 7 shows a droplet in the 53–38 µm size fraction, with dispersoids being noticeably smaller than 1 µm.

Notably, the size distribution of dispersoids in any chosen dendrite arm appears relatively uniform, without a massive variation where one dispersoids grows at the expense of others nearest to it. Furthermore, we do not observe a significant reduction in occurrence rate of solid-state dispersions at very high cooling rates in $CoCrCuFeNi_{0.8}$ droplets. Solid-state dispersions in dendrites are instead almost ubiquitous in the smallest size fraction produced (53–38 µm). We hypothesise therefore, that even at the highest cooling rates encountered in this experiment, where solid-state decomposition is kinetically greatly hindered, the driving force for the decomposition created by the undercooling of the alloy is high enough that solid-state dispersions will still form. If, indeed, there exists a cooling rate at which formation of the copper-rich solid can be supressed, it is likely in excess of 60,000 K s^{-1}.

Given this inability to supress the decomposition reaction, and the relatively uniform size distribution of dispersoids within any specific dendrite arm, we suggest that the dispersoids formed in the dendrite cores are more likely the result of a spinodal decomposition reaction than one requiring nucleation and growth. However, more experimental work is required to define the reaction mechanism with certainty.

The inset in Fig. 7 shows a magnified view of solid-state dispersions of copper-rich phase within the HEA dendrite trunk. We attribute the presence of darker spots on the periphery of most of these dispersoids to voids being formed in the material. Given the heavy presence of shrinkage porosity in the copper-rich interdendritic phase, we assume that a similar process has occurred within many of the copper-rich dispersoids.

Large Dispersions—Liquid Phase Separation

As discussed in "Structural Trend Analysis—Large Dispersions" section, we hypothesise that the large dispersion structures form as a result of LPS in the alloy melt before solidification.

We see these structures primarily in droplets with diameters between 300 and 100 µm and corresponding cooling rates between 5000 and 15,000 K s^{-1}. This higher prevalence at intermediate cooling rates mimics the peak in core–shell incidence in binary alloys, although in this study, these

dispersions appear much less often in general, occurring in less than 10% of the droplets even in size fractions where they are most common.

Contrary to work with binary alloys, where at the highest cooling rates, LPS presents in the form of fine dispersions of MPDs across the whole droplet diameter, the large dispersions we observe never occupy the entire droplet, even at the smallest size fractions. Instead, dispersions usually seem to originate from the edge of the droplet and occupy between 10 and 40% of the final microstructure cross section. Examples of continuous and cellular large dispersion structures are shown in Fig. 4e and f, respectively.

This dispersion pattern is not unlike that found in the highest cooling rate areas of the arc-melted ingot. Dispersions primarily occur at the edge of the droplet with the solidification direction appearing to be inwards from these points. In contrast to continuous dispersions, cellular dispersions are surrounded by a web-like structure of copper-rich phase.

We suggest that the occurrence of large dispersion structures as the only form of LPS in the alloy is due, in part, to the low volume fraction of the copper-rich phase present in the alloy. Because there is so little copper-rich phase, and so little time for coarsening and movement due to Marangoni convection due to high prevailing cooling rates, it becomes impossible for dispersions of MPDs to consolidate and form more conventional LPS structures observed in binary and ternary alloys. This phenomenon is discussed further in "Drop-Tube-Processed CoCrCuFeNi0.8—Comparison with Binary Co–Cu" section.

Spontaneous Grain Refinement

Another notable solidification trend in $CoCrCuFeNi_{0.8}$ is the presence in all size fractions of what appear to be partially and fully grain-refined microstructures.

Spontaneous grain refinement is an observed transformation in undercooled metallic melts, whereby the final solidified microstructure changes from exhibiting larger and/or columnar grains to much finer equiaxed grains [51]. The behaviour has been consistently reported in the literature since it was first described and studied by Walker [52]. It has been observed repeatedly in work on rapid solidification in pure elements [53], binary systems including Cu–Ni, Cu–O, Cu–Sn, Ni_3–Al and Ag–O [4, 54–57] as well as high-entropy alloys such as $Al_{0.3}CoCrFeNi$ [58] and CoFeNiPd [59].

Many mechanisms have been put forward in the last few years to describe the occurrence of spontaneous grain refinement during solidification of metallic melts. One of the most recent and commonly accepted theories from Schwarz et al. revolves around dendrite fragmentation of already-solidified dendrites after recalescence due to melt disturbance caused by stirring or melt flow [60, 61]. Other work points to fragmentation occurring during (rather than after) recalescence, and preferential remelting of unstable intermediate "dendritic seaweed" structures to form the grain-refined morphology [4, 53, 54, 56, 62]. Of great importance is a critical undercooling to facilitate this change in structure during solidification. While pure metal melts tend to exhibit one transition from columnar grains to finer scale equiaxed grains at a specific undercooling ΔT^* [53], it has been found that many alloy systems show two transitions, where spontaneous grain refinement occurs at a lower undercooling ΔT_1, followed by a return to regular columnar dendritic morphology. Once a higher critical undercooling ΔT_2 is reached, another independent transition to fine equiaxed grains is observed, a second episode of spontaneous grain refinement [54, 57, 63, 64].

We note the extensive presence of grain refinement in either an intermediate or more complete form in all size fractions of solidified $CoCrCuFeNi_{0.8}$. Percentage incidence of any grain refinement in these droplets peaks at the second largest size fraction (droplets between 500 µm and 850 µm in diameter) at about 50% of analysed droplets. Partial grain refinement is present in all droplet size fractions. Fully grain-refined structures are found only in the largest five size fractions down to the 212–150 µm size fraction, meaning that the fully grain-refined structures fail to form at prevailing cooling rates above some 10,000 K s^{-1}. The stochastic nature of undercooling, however, means that droplets of any size fraction may achieve the required undercooling to undergo at least partial grain refinement. Additionally, grain refinement is also generally less prevalent in drop-tube samples than it is in electromagnetic levitation (EML) or refluxing experiments. This can be because of comparatively higher cooling rates occurring in the drop tube which inhibit the process, as well as the absence of an induced magnetic field, which removes the effect of forced convection during the solidification process. We use these concepts to understand why partial grain refinement persists, albeit at lower occurrence rates, throughout the droplet size fractions and cooling rates, rather than in only very specific discrete droplet sizes.

Notably, after the initial peak in occurrence rate of grain-refined structures at relatively low cooling rates below 5000 K s^{-1}, there is also an uptick in the incidence of partially grain-refined structures in the smallest size fraction and highest cooling rates (~60,000 K s^{-1}). This phenomenon suggests two different mechanisms being responsible for grain refinement at low and high cooling rates (and, respectively, low and high undercoolings), in line with the observation of ΔT_1 and ΔT_2 critical undercoolings in other alloy systems. Due to uncertainty in identification at small size fractions and the low sample size compared to the whole, this trend should only be seen as tentative, and more droplets should be evaluated before this relationship is conclusively

proven or disproven. However, even without this definitive data, the fact that the prevalence of spontaneous grain refinement decreases after peaking at intermediate droplet sizes indicates that we are observing an alloy ΔT_1 refinement transition. In pure element systems, a decrease in occurrence does not occur. Fine equiaxed grains persist after a single transition from columnar to equiaxed grains at one critical undercooling ΔT^*.

We suggest, whatever mechanism is responsible for grain refinement in this cooling regime and/or material, that fully grain-refined structures are not observed below a certain droplet size due to a decrease in time during which prevailing droplet temperature is high enough for the diffusion of solute to facilitate the refinement process (i.e. when the solid and liquid co-exist) or for the remelting process.

Summary of Solidification Structures and Timeline of Occurrence

The relationship between the four primary structures created during drop-tube processing of the $CoCrCuFeNi_{0.8}$ alloy (conventional dendritic solidification, LPS, solid-state decomposition, and spontaneous grain refinement) is worth discussing given the presence of many droplets featuring more than one of these microstructures and the impact of one microstructure on the other. The occurrence percentage of the primary categories of microstructure is shown in Fig. 11 to indicate the cooling rate at which particular structures are most likely to form. This represents the beginning of a map from which a desired microstructure can be selected during rapid solidification processing using methods such as drop-tube processing or industrial methods such as gas atomisation. A schematic of the process of structural formation in various solidification scenarios is represented in Fig. 12. Here, the liquidus and solidus are marked to begin to hypothesise when each structure begins to form. For instance, LPS would naturally occur before the onset of solidification, but temperature would be below the liquidus given that LPS is likely metastable in this alloy. Conversely, formation of solid-state dispersions would likely occur after temperature falls below the solidus temperature and solidification is complete.

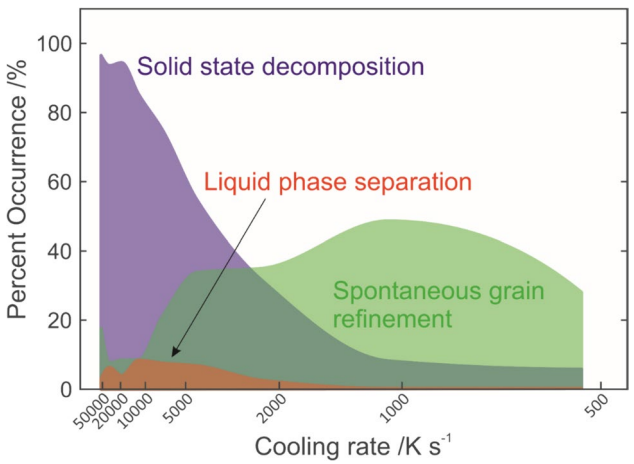

Fig. 11 Summary of likelihood of obtaining specific droplet microstructures through alteration of cooling rate in drop-tube-processed rapidly solidified $CoCrCuFeNi_{0.8}$

Any LPS would occur, obviously, in the liquid state in lieu of conventional dendritic solidification. When undercooling is raised above a critical value ΔT_{LPS} under the liquidus, a new copper-rich phase nucleates in the parent liquid in the form of MPDs. In this alloy, MPDs do not occupy the entire microstructure, largely due to the low volume fraction of copper-rich phase. Instead, they are limited to one region in the microstructure. Most droplets suggested to have undergone LPS share the microstructure with dendrites. The structures seem to mostly consist of a region of liquid separation from which dendrites originate and radiate outwards. This can be seen in Fig. 4e and f. The directional solidification points to LPS occurring before dendritic solidification, supporting the idea that these dispersions are formed in the liquid state. As undercooling decreases back below ΔT_{LPS} the remaining liquid present in the droplet solidifies in a dendritic manner, with copper-lean dendrites growing into the remaining liquid. This liquid gradually becomes enriched with copper. Given that LPS occurs most readily at cooling rates above some 5000 K s^{-1}, it is likely that this cooling rate begins to allow undercooling to reach ΔT_{LPS} at an appreciable occurrence rate. If no LPS occurs, the droplet solidifies dendritically, with copper-lean dendrites growing into a liquid that subsequently becomes enriched in copper.

Given that spontaneous grain refinement is likely caused by dendrite fragmentation and/or remelting during or just after recalescence, it is assumed that this occurs just after the onset of dendritic solidification. When prevailing cooling rates rise to above 1000 K s^{-1}, critical undercooling required for the first instance of spontaneous grain refinement, ΔT_1, is reached. From here, grain refinement occurs and solidifying dendrites fragment or re-melt into an equiaxed structure. This structure solidifies into place once temperature dips below the solidus.

Solid-state decomposition, occurring entirely in the solid state, likely occurs after initiation of grain refinement or LPS, or after the initiation of dendritic solidification in the droplet. This is assumed to be caused by supersaturation of copper caused by high undercooling of the sample. Because rapid cooling causes a high prevailing undercooling, dendrite growth velocity is increased. Solute trapping is enhanced when the velocity of the growth front approaches the diffusion velocity of solute (in this case, mostly copper) across the interface. Therefore, dendrites that grow, and refine, are likely supersaturated with copper. Once temperature drops

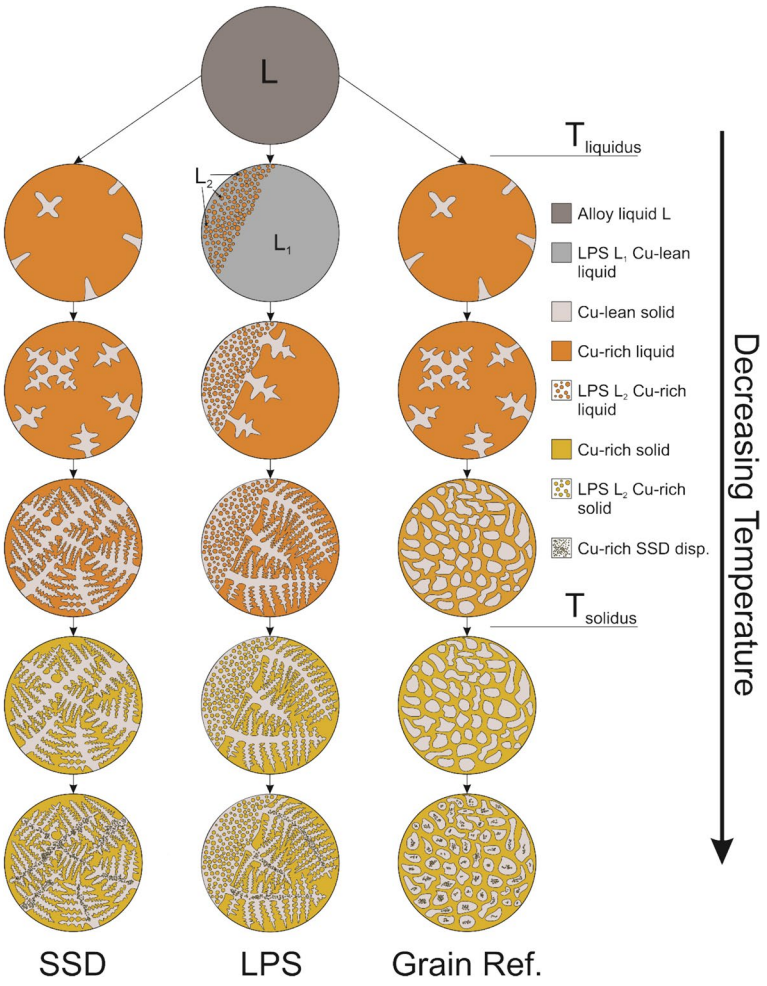

Fig. 12 Schematic of structural formation of solid-state dispersions (SSD), liquid phase separation (LPS) dispersions and spontaneous grain refinement (Grain Ref.) in drop-tube-processed $CoCrCuFeNi_{0.8}$

below a certain value below the solidus, a decomposition reaction is initiated and the copper-rich dispersoids form within the solidified dendrite arms. Importantly, solid-state dispersions are not only present in primary dendrites, but also in grain-refined equiaxed grains or intermediate structures seen in droplets classified as partially or fully grain refined. Because a grain-refined structure likely consists of fragmented or partially remelted dendrites, the supersaturation is likely also present within these grains, leading to decomposition in the grain centres.

Grain refinement and solid-state dispersions have been observed occurring separately or together in droplets across size fractions. They may also both not occur at all in certain droplets. We suggest, therefore, that the occurrence of each structure is independent of the occurrence of the other.

Drop-Tube-Processed $CoCrCuFeNi_{0.8}$—Comparison with Binary Co–Cu

Although drop-tube experiments do not allow for the direct measurement of undercooling prior to solidification, the high obtainable cooling rates have been proven to undercool alloys far enough below the liquidus to facilitate metastable LPS. Mullis et al. [17] have formulated a method through which to calculate undercooling at the point of LPS and the point of solidification in Co–Cu alloys. These alloys are similar to $CoCrCuFeNi_{0.8}$ in melting point and other thermophysical properties such as density and heat capacity [24]. Therefore, we conjecture that undercooling reached in droplets of $CoCrCuFeNi_{0.8}$ upon solidification is similar to that of the drop-tube-processed binary Co–Cu. This suggests undercoolings of below 50 K in the largest droplets and up to some 300 K in the smallest droplets. However, despite a thermophysical similarity, solidification and phase separation have not proceeded in $CoCrCuFeNi_{0.8}$ in the same way as binary alloys like Co–Cu. In addition, while common in binary alloy studies, core–shell structures have only rarely been observed at all during rapid solidification of HEAs. In a study by Zhang et al. [65], for example, inoculant Y_2O_3 particles were required to facilitate nucleation of LPS in laser-cladded $AlCoCrCuFeNiSi_{0.5,}$ and produce core–shell structures. A comparison between microstructural evolution in

drop-tube-processed $CoCrCuFeNi_{0.8}$ and binary Co–Cu, as well as reasons for key differences, is therefore explored here.

Like Co–Cu, dendritic solidification predominates at high size fractions. The reason for this behaviour in both alloys is likely the same. Cooling rates are too low to facilitate undercooling required for binodal LPS. The near-equilibrium conditions therefore facilitate dendritic solidification.

At intermediate size fractions, however, core–shell microstructures which form a significant fraction of microstructures present in Co–Cu droplets [24], are almost never present in the $CoCrCuFeNi_{0.8}$ droplets solidified in this study, other than 3 or 4 isolated cases among thousands of droplets. Any LPS in $CoCrCuFeNi_{0.8}$ is present as fine dispersions of copper-rich L_2 droplets.

For core–shell structures to form, multiple requirements must be satisfied. First, LPS must occur initially, in that the metastable miscibility gap must be accessed to begin with. The fact that there are droplets exhibiting unorthodox structures, particularly the large continuous and cellular dispersions, indicates that sufficient undercooling has been achieved to facilitate LPS. Furthermore, the driving force for Marangoni convection must be high enough to cause appreciable movement of MPDs, facilitating core–shell formation through coalescence. This driving force is provided by the interfacial energy between the phases. Owing to the large melting point difference between the copper-rich and HEA phase in this alloy, it is assumed that this condition is satisfied. Finally, time for nucleation, growth and coalescence of L_2 MPDs into core–shell structures is constrained by the interval between initial LPS and the onset of solidification. To enhance formation ability, we can either increase the rate at which these processes occur, or increase the time interval within which they proceed. We must therefore discuss variables which may impact nucleation, growth and coalescence of the copper-rich minority L_2 phase in $CoCrCuFeNi_{0.8}$ compared to Co–Cu binary alloys.

The first possible limiting factor for core–shell formation lies in the volume ratio of the liquid phases. Studies on equiatomic CoCrCuFeNi show that the majority of copper segregates into the interdendritic phase upon solidification [18, 26, 27, 29–31, 33]. Importantly, however, the copper-rich phase only typically occupies an extremely small volume fraction in the microstructure. This is only slightly impacted by undercooling. For example, Wang et al. observe a volume fraction of the HEA dendritic phase at 92.5% at 0 K of undercooling, leaving only a maximum volume fraction of 7.5% for the copper-rich interdendritic phase. At the maximum undercooling of 381 K, the total volume fraction of the copper-rich phase increases only to a maximum of 12–13% [29]. The volume fraction ratio of the dendritic HEA phase to the copper-rich interdendritic phase in the $CoCrCuFeNi_{0.8}$ produced in this study is only about 88:12 in the ingot sample and a very similar 86:14 in droplet samples, very different from those observed binary alloys similar binary alloys (e.g. Co–Cu). This likely poses a problem for coalescence of nucleated MPDs. In Co–Cu, Jegede et al. [24] produced the best conditions for core–shell formation when copper-rich and cobalt-rich phases formed with volume fraction ratios closer to 50:50. Robinson et al. [66] have also studied undercooled Co–Cu alloys, and note that core–shell structures only appear when the volume fraction of the minority phase is over 20%. The largest forming MPDs form only at compositions, where the volume fraction each of the phases is similar. At the extremes, fine dispersions result. The authors attribute this to composition as well as undercooling. While higher undercooling naturally refines the microstructure, composition deviating too far from that at which the volume fractions of the two phases are near-equal raises the time required for the MPDs to coalesce into core–shell structures. Wang et al. [39] observe similar behaviour in stable LPS binary alloys, where the MPD sizes increased when composition was near the critical point and more time was available between LPS and solidification for forces such as Marangoni convection to form core–shell structures.

The velocity of Marangoni motion may also be important to discuss. Working on a drop-tube-processed Fe–Cu–Sn ternary alloy, Wang et al. [67] developed a phase field model, which predicts that Marangoni movement velocities of MPDs increase with increasing size of the said droplet/globule. This occurs regardless of the overall diameter of the drop-tube-processed alloy droplet. A reduction in effectiveness of Marangoni convection on smaller MPDs could also be an explanation for a lack of core–shell formation.

Even more fundamentally, given that LPS in the binodal form proceeds via a nucleation and growth mechanism, we conjecture that the addition of more elements to a binary alloy may also actually inhibit nucleation of MPDs. Copper, as discussed, is the primary de-mixing element in $CoCrCuFeNi_{0.8}$. Therefore, in binodal LPS, MPDs of copper-rich liquid must nucleate in the parent liquid. Relating this to classical nucleation theory, the precursor to nucleation would comprise of small clusters of atoms of new phase within the original. During binodal LPS, a copper-rich cluster would therefore need to form in the parent liquid, requiring a specific number of copper atoms in close proximity to form a cluster of sufficient size [68]. We therefore reason that a lower atomic percent of copper in the alloy would lower the probability that an adequately large minority phase embryo of copper-rich liquid would occur stochastically in the parent liquid for nucleation to proceed. Hence, both nucleation and coalescence of MPDs could be impacted by a lower prevalence of copper-rich L_2 phase in $CoCrCuFeNi_{0.8}$ compared to a binary alloy such as equiatomic Co–Cu.

Another possible explanation for lack of core–shell formation is the sluggish diffusion phenomenon in HEAs. This could particularly affect the growth of MPDs after nucleation. In their study of laser-cladded $AlCoCrCuFeNiSi_{0.5}$, Zhang et al. [65] suggest this as one of the causes of "low sphericity" or incomplete core–shell formation in their alloy.

Sluggish diffusion is one of the theorised core effects in HEAs that distinguishes them from more conventional binary alloys. With an increasing number of constituent elements, variable bond energies cause drastic differences in lattice potential energy across the material, lowering the efficacy with which solute diffusion can occur [69]. This is more readily accepted in solid alloys but has been suggested to occur in metallic melts due to the presence of short-range order within the liquid.

Kurtuldu et al. [70] have studied the impact of short-range order on the diffusion of elements in alloy melts, finding that the addition of Cr to an Al–Zn melt slows diffusion of Zn atoms through the liquid. They attribute this slowing to the formation of icosahedral short-range order in the melt due to the addition of Cr. To our knowledge however, similar work has yet to be done on HEAs. We note, therefore, that the argument for sluggish diffusion in HEAs is ongoing, somewhat controversial, and, to our knowledge, has only been readily investigated experimentally in the solid state [71]. More experimentation must be done before lack of core–shell morphology in drop-tube-processed $CoCrCuFeNi_{0.8}$ can be attributed to such a phenomenon.

Finally, another area of similarity between $CoCrCuFeNi_{0.8}$ and Co–Cu is the presence of fine dispersion LPS structures and hybrid structures consisting of fine dispersions and dendrites. These structures are formed most often at higher cooling rates in Co–Cu. In the examined $CoCrCuFeNi_{0.8}$ droplets, LPS dispersions become prevalent at a minimum cooling rate of 1000 K s^{-1} (although statistical analysis of their prevalence in $CoCrCuFeNi_{0.8}$ shows a slight decrease in occurrence at the very highest cooling rates). Their formation at high cooling rates likely reflects a prohibitively small-time interval between LPS and solidification as mentioned in "Large dispersions—liquid phase separation" section. Indeed, even in equiatomic Co–Cu, the droplet simply cools too quickly to allow for the formation of a core–shell structure via the coalescence, no matter how optimal volume fraction of the co-existing liquid phases is for such coalescence [24].

Conclusion

Almost 2500 droplets have been analysed during this investigation on drop-tube-processed $CoCrCuFeNi_{0.8}$. A test of only one composition solidified at varying cooling rates yields a striking number of structural morphologies as well as hybrid structures. Occurrence of LPS is very uncommon compared to drop-tube-processed binary immiscible alloys, with incidence of peaking at only 8% at intermediate cooling rates between 5000 and 12,000 K s^{-1}. Other than two cases of core–shell formation, only large fine dispersions are observed. At lower cooling rates below 5000 K s^{-1} the alloy solidifies largely dendritically. In some of these droplets, spontaneous grain refinement also occurs, with a dendritic microstructure transforming into fine equiaxed grains. As cooling rate increases, higher undercooling leads to enhanced supersaturation of solidifying dendrites. After solidification, a solid-state decomposition reaction is initiated with copper-rich dispersoids forming throughout the cores of dendrite arms and the centres of equiaxed grain-refined grains in grain-refined droplets. Occurrence of these dispersions increases monotonically, and they feature in almost all droplets solidified at cooling rates above 20,000 K s^{-1}. The fact that multiple different microstructures can all be present in one droplet indicates that the occurrence of one structure is likely independent of the others.

Comparison with similar rapid cooling experiments on binary immiscible alloys reveals a similarity in some obtainable structures, particularly dendritic structures at lower cooling rates and finely dispersed liquid phase separated structures at higher cooling rates. However, the core–shell structures that are highly prevalent in alloys such as Co–Cu are all but absent in similarly processed $CoCrCuFeNi_{0.8}$. We attribute this difference to the extremely low volume fraction of the minority phase formed in $CoCrCuFeNi_{0.8}$ after liquid phase separation. This, along with the high cooling rates in drop-tube processing, means nucleated MPDs do not have enough time to coalesce into core–shell structures before solidification, and instead remain as fine dispersions.

Outlook

This initial investigation into microstructures yielded in drop-tube-processed $CoCrCuFeNi_{0.8}$ reveals numerous avenues for future exploration. The solid-state decomposition that has occurred in the primary dendrite arms is worthy of further analysis to decisively confirm formation mechanisms and to explore potential impacts on mechanical properties of the alloy. Such a localised dispersion structure has seldom been observed in HEAs. The same can be said for the spontaneous grain refinement we have catalogued. $CoCrCuFeNi_{0.8}$ can thus also provide a good candidate for further investigations into mechanisms for grain refinement in HEAs, which have not been as extensively studied as in binary alloys. In terms of comparison to behaviour of immiscible binary alloys, we may begin to use this study to understand why desirable core–shell structures might be harder to achieve in HEAs. From the discussion surrounding the reasons for a

lack of core–shell formation, we can therefore begin to tailor the composition, phase volume fraction and experimental conditions to increase the likelihood of core–shell formation in rapidly solidified HEAs should such structures be desirable for industrial use. Additionally, exploration into the controversial sluggish diffusion phenomenon in HEAs, particularly in the liquid state, would further elucidate the impact that the addition of elements has on the behaviour of immiscible alloys.

Appendix 1: Minimum Sample Size Determination and Uncertainty Quantification for Statistical Analysis of Microstructure Prevalence

Minimum Sample Size Determination

Viewable, and therefore classifiable droplets, particularly in the case of smaller size fractions, often number in the hundreds or even thousands. Statistically, a large sample size is favourable for determining trends across samples with any degree of certainty. Therefore, we establish a minimum sample size (n) for droplet sieve fractions in situations, where it was deemed unfeasible to count all exposed droplets (i.e. all droplet sieve fractions other than the two largest). To determine a minimum sample size, one sieve fraction was chosen at random (53–75 µm) and the structures of 514 droplets were catalogued.

From the sample, of size $n = 514$, we construct two subsamples of size g, where $15 \leq g \leq 257$. We then compare the numeric incidence of each of the 18 original classification types listed in "Structural classification and analysis" section, calculating the absolute value of the difference between the incidence of each structure within the two subsets. From this, a percentage similarity between the two subsets may be constructed. This procedure is then repeated for 100 different randomisations for each value of g so as to smooth out sampling noise and provide an average similarity between samples as a function of sample size. This is shown in Fig. 13, with sample sizes under $n = 30$ ($g = 15$) being omitted due to the tendency for drastically different results between trials (i.e. sample sizes of $n = 2$ would either produce a 100% or 0% difference). Also shown is a logarithmic fitting curve which, as can be seen, is a good model for the data. Based on the trend, increasing the sample size n from 250 to 500 is likely to result only in a 5–10% increase in similarity. We conclude that, for the other size fractions, a count above $n = 250$ is unnecessary given the time required to gather such data.

Other size fractions, which present a different spread of structures than that observed in the 53–75 µm sieve fraction, can also be treated with this analysis method.

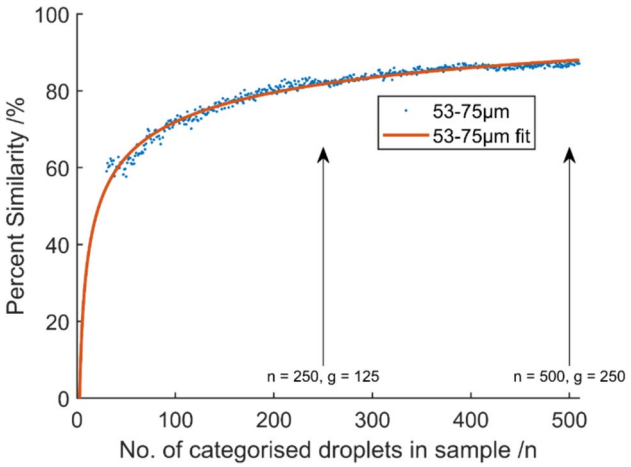

Fig. 13 Percent similarity variation with sample size in 53–75 µm size fraction of $CoCrCuFeNi_{0.8}$ droplets

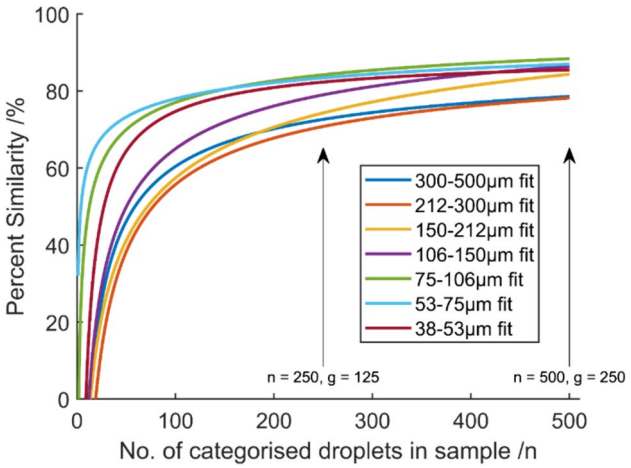

Fig. 14 Percent similarity as a function of sample size for droplet size fractions of $CoCrCuFeNi_{0.8}$

However, as we have only analysed around 250 droplets in each of the other sieve fraction, a logarithmic fit was used to extrapolate to a sample size $n = 500$. Results are shown in Fig. 14. Importantly, the 850+ µm and 500–850 µm size fractions had a total of less than 250 countable droplets, meaning that this extrapolation was not necessary for these two size fractions, as the whole exposed population could be classified. The final similarity values are an average calculated after simulating the randomisation of the samples five times. The maximum increase in similarity yielded when doubling the sample size is lower than 10% in all sieve fractions. With a percent similarity of already > 70% across all size fractions, we conclude that increasing the sample size beyond $n = 250$ is unnecessary.

Uncertainty Quantification

To estimate the measurement uncertainty in the incidence of structures across the different sieve fractions, we assume the sample can be modelled by a binomial distribution with a 95% confidence interval. That is in a sample of size n, what is the chance of getting k droplets of a particular type, given the probability of such a droplet being selected at random is p.

The key assumption of the binomial distribution is that each selection must be indepon is that each selection must be independent. Here, however, we estimate the probability of a given structure occurring in the sample based on its actual measured occurrence during categorisation i.e. $p = k_{\text{obs}}/n$, where k_{obs} is the observed incidence of that structure. This approach is an approximation because the probability of success (i.e. the chance of picking a droplet with the desired structure) is informed by the nature of the sample and thus, not strictly independent of the sample itself. However, we contend that its use gives sufficient indication of the likely error in the sample. The modified version of the binomial equation is shown in Eq. 1.

$$B_n(k) = \binom{n}{k}\left(\frac{k_{\text{obs}}}{n}\right)^k\left(1-\frac{k_{\text{obs}}}{n}\right)^{n-k}. \quad (1)$$

To find a confidence range, and thus delineate uncertainty in the incidence of certain structures in a sample, we ask "in a sample of n droplets, where k_{obs} droplets possess the structure we desire, what are the values of k above and below k_{obs} where, if it were guessed that the structure chosen was that which was desired, we would be right 95% of the time?". Setting the value of $B_n(k)$ to 0.95 and solving for the two possible values of k for each structure type and each sieve fraction gives the confidence intervals on the incidence of the desired structure. For example, if 100 droplets from a sample of 250 are found to possess the selected structure, using 250 for n and 10/25 for p, assuming $B_n(k) = 0.95$, yields 94 and 107. These then form the upper and lower uncertainty bounds on the incidence of that structure. This method is used to generate the error bars in Figs. 8, 9 and 10.

Supplementary Information The online version contains supplementary material available at https://doi.org/10.1007/s44210-024-00039-x.

Acknowledgements This work was supported by an Engineering and Physical Sciences Research Council (EPSRC) Doctoral Training Partnership (DTP) Scholarship.

Author Contributions Liam Teggin: Conceptualisation, data curation, formal analysis, investigation, methodology, software, visualisation, validation and writing—original draft. Robert Cochrane: Conceptualisation, formal analysis, methodology, supervision and writing—review and editing. Andrew Mullis: Conceptualisation, formal analysis, methodology, software, supervision and writing—review and editing.

Data Availability Raw data collected for the purposes of this investigation are available via the White Rose Repository (https://eprints.whiterose.ac.uk).

Declarations

Competing interests The authors declare that they have no known competing financial interests or personal relationships that could have appeared to influence the work reported in this paper.

Open Access This article is licensed under a Creative Commons Attribution 4.0 International License, which permits use, sharing, adaptation, distribution and reproduction in any medium or format, as long as you give appropriate credit to the original author(s) and the source, provide a link to the Creative Commons licence, and indicate if changes were made. The images or other third party material in this article are included in the article's Creative Commons licence, unless indicated otherwise in a credit line to the material. If material is not included in the article's Creative Commons licence and your intended use is not permitted by statutory regulation or exceeds the permitted use, you will need to obtain permission directly from the copyright holder. To view a copy of this licence, visit http://creativecommons.org/licenses/by/4.0/.

References

1. D. Fisher, M. Rappaz, W. Kurz, Fundamentals of solidification, in *Fundamentals of Solidification* (Trans Tech Publications, Baech, 2023), pp. 1–353
2. Y. Zhang, B. Huang, J. Li, Microstructural evolution with a wide range of solidification cooling rates in a Ni-based superalloy. Metall. Mater. Trans. A. **44**, 1641–1644 (2013)
3. Z. Chen, Y. Lei, H. Zhang, Structure and properties of nanostructured A357 alloy produced by melt spinning compared with direct chill ingot. J. Alloys Compd. **509**(27), 7473–7477 (2011)
4. E.G. Castle, A.M. Mullis, R.F. Cochrane, Mechanism selection for spontaneous grain refinement in undercooled metallic melts. Acta Mater. **77**, 76–84 (2014)
5. A.F. Andreoli, O. Shuleshova, V.T. Witusiewicz, Y. Wu, Y. Yang, O. Ivashko, A.-C. Dippel, M.V. Zimmermann, K. Nielsch, I. Kaban, In situ study of non-equilibrium solidification of CoCrFeNi high-entropy alloy and CrFeNi and CoCrNi ternary suballoys. Acta Mater. **212**, 116880 (2021)
6. J. Vitek, A. Dasgupta, S. David, Microstructural modification of austenitic stainless steels by rapid solidification. Metall. Trans. A **14**, 1833–1841 (1983)
7. H. Jones, Formation of metastable crystalline phases in light-metal systems by rapid solidification. Philos. Mag. B **61**(4), 487–509 (1990)
8. F. Hehmann, F. Sommer, B. Predel, Extension of solid solubility in magnesium by rapid solidification. Mater. Sci. Eng. A **125**(2), 249–265 (1990)
9. P.M. Smith, M.J. Aziz, Solute trapping in aluminum alloys. Acta Metall. Mater. **42**(10), 3515–3525 (1994)
10. R. Willnecker, D. Herlach, B. Feuerbacher, Evidence of non-equilibrium processes in rapid solidification of undercooled metals. Phys. Rev. Lett. **62**(23), 2707 (1989)
11. B. Vishwanadh, N. Sarkar, S. Gangil, S. Singh, R. Tewari, G. Dey, S. Banerjee, Synthesis and microstructural characterization of a novel multicomponent equiatomic ZrNbAlTiV high entropy alloy. Scripta Mater. **124**, 146–150 (2016)
12. S. Gorsse, C. Hutchinson, M. Gouné, R. Banerjee, Additive manufacturing of metals: a brief review of the characteristic

microstructures and properties of steels, Ti–6Al–4V and high-entropy alloys. Sci. Technol. Adv. Mater. **18**(1), 584–610 (2017)
13. O. Oloyede, T.D. Bigg, R.F. Cochrane, A.M. Mullis, Microstructure evolution and mechanical properties of drop-tube processed, rapidly solidified grey cast iron. Mater. Sci. Eng. A **654**, 143–150 (2016)
14. Y. Lv, R. Hu, Z. Yao, J. Chen, D. Xu, Y. Liu, X. Fan, Cooling rate effect on microstructure and mechanical properties of AlxCoCrFeNi high entropy alloys. Mater. Des. **132**, 392–399 (2017)
15. P. Sreeramagiri, A. Roy, G. Balasubramanian, Effect of cooling rate on the phase formation of AlCoCrFeNi high-entropy alloy. J. Phase Equilib. Diffus. **42**(5), 772–780 (2021)
16. A. Nassar, A. Mullis, R. Cochrane, Z. Aslam, S. Micklethwaite, L. Cao, Rapid solidification of $AlCoCrFeNi_{2.1}$ high-entropy alloy. J. Alloys Compd. **900**, 163350 (2022)
17. A.M. Mullis, O.E. Jegede, T.D. Bigg, R.F. Cochrane, Dynamics of core–shell particle formation in drop-tube processed metastable monotectic alloys. Acta Mater. **188**, 591–598 (2020)
18. N. Derimow, R. Abbaschian, Liquid phase separation in high-entropy alloys—a review. Entropy **20**(11), 890 (2018)
19. Y. Nakagawa, Liquid immiscibility in copper–iron and copper–cobalt systems in the supercooled state. Acta Metall. **6**(11), 704–711 (1958)
20. R. Dai, S. Zhang, J. Li, One-step fabrication of Al/Sn–Bi core–shell spheres via phase separation. J. Electron. Mater. **40**(12), 2458 (2011)
21. R. Dai, J. Zhang, S. Zhang, J. Li, Liquid immiscibility and core-shell morphology formation in ternary Al–Bi–Sn alloys. Mater. Charact. **81**, 49–55 (2013)
22. M. Li, P. Jia, X. Sun, H. Geng, M. Zuo, D. Zhao, Liquid–liquid phase equilibrium and core–shell structure formation in immiscible Al–Bi–Sn alloys. Appl. Phys. A **122**, 1–6 (2016)
23. L. Ratke, S. Diefenbach, Liquid immiscible alloys. Mater. Sci. Eng. R. Rep. **15**(7–8), 263–347 (1995)
24. O.E. Jegede, R.F. Cochrane, A.M. Mullis, Metastable monotectic phase separation in Co–Cu alloys. J. Mater. Sci. **53**(16), 11749–11764 (2018)
25. N. Yan, Z. Hong, D. Geng, B. Wei, A comparison of acoustic levitation with microgravity processing for containerless solidification of ternary Al–Cu–Sn alloy. Appl. Phys. A **120**(1), 207–213 (2015)
26. N. Derimow, R. Abbaschian, Solidification microstructures and calculated mixing enthalpies in CoCrCu containing alloys. Mater. Today Commun. **15**, 1–10 (2018)
27. N. Liu, P. Wu, P. Zhou, Z. Peng, X. Wang, Y. Lu, Rapid solidification and liquid-phase separation of undercooled CoCrCuFexNi high-entropy alloys. Intermetallics **72**, 44–52 (2016)
28. P. Wu, N. Liu, W. Yang, Z. Zhu, Y. Lu, X. Wang, Microstructure and solidification behavior of multicomponent CoCrCuxFeMoNi high-entropy alloys. Mater. Sci. Eng. A **642**, 142–149 (2015)
29. W. Wang, L. Hu, S. Luo, L. Meng, D. Geng, B. Wei, Liquid phase separation and rapid dendritic growth of high-entropy CoCrCuFeNi alloy. Intermetallics **77**, 41–45 (2016)
30. T. Guo, J. Li, J. Wang, Y. Wang, H. Kou, S. Niu, Liquid-phase separation in undercooled CoCrCuFeNi high entropy alloy. Intermetallics **86**, 110–115 (2017)
31. W. Wang, Z. Kong, Phase separation and microhardness of rapidly solidified high-entropy CoCrFeNiCux alloys. J. Alloys Compd. **853**, 156451 (2021)
32. K. Lin, C. Wei, Y. He, C. Li, P. Zhang, J. Li, J. Wang, Formation of core–shell structure in immiscible $CoCrCuFe_{1.5}Ni_{0.5}$ high-entropy alloy. Mater. Lett. **321**, 132452 (2022)
33. P. Wu, N. Liu, P. Zhou, Z. Peng, W. Du, X. Wang, Y. Pan, Microstructures and liquid phase separation in multicomponent CoCrCuFeNi high entropy alloys. Mater. Sci. Technol. **32**(6), 576–580 (2016)
34. A. Munitz, M. Kaufman, R. Abbaschian, Liquid phase separation in transition element high entropy alloys. Intermetallics **86**, 59–72 (2017)
35. X. Liu, X. Lu, B. Wei, Rapid monotectic solidification under free fall condition. Sci. China Ser. E Technol. Sci. **47**(4), 409–420 (2004)
36. E.A. Brandes, G. Brook, *Smithells Metals Reference Book* (Elsevier, Amsterdam, 2013)
37. D. Bonnell, J. Treverton, A. Valerga, J. Margrave, The emissivities of liquid metals at their fusion temperatures, in *Proceedings of the 5th Symposium on Temperature* (1972)
38. E.-S. Lee, S. Ahn, Solidification progress and heat transfer analysis of gas-atomized alloy droplets during spray forming. Acta Metall. Mater. **42**(9), 3231–3243 (1994)
39. N. Wang, L. Zhang, Y. Peng, W. Yao, Composition-dependence of core-shell microstructure formation in monotectic alloys under reduced gravity conditions. J. Alloys Compd. **663**, 379–386 (2016)
40. Z. Peng, N. Liu, S. Zhang, P. Wu, X. Wang, Liquid-phase separation of immiscible CrCu x FeMo y Ni high-entropy alloys. Mater. Sci. Technol. **33**(11), 1352–1359 (2017)
41. S. Wang, Z. Chen, L. Feng, Y. Liu, P. Zhang, Y. He, Q. Meng, J. Zhang, Nano-phase formation accompanying phase separation in undercooled CoCrCuFeNi–3 at.% Sn high entropy alloy. Mater. Charact. **144**, 516–521 (2018)
42. A. Munitz, M. Kaufman, J. Chandler, H. Kalaantari, R. Abbaschian, Melt separation phenomena in CoNiCuAlCr high entropy alloy containing silver. Mater. Sci. Eng. A **560**, 633–642 (2013)
43. M. Rahul, S. Samal, G. Phanikumar, Metastable microstructures in the solidification of undercooled high entropy alloys. J. Alloys Compd. **821**, 153488 (2020)
44. U. Hsu, U. Hung, J. Yeh, S. Chen, Y. Huang, C. Yang, Alloying behavior of iron, gold and silver in AlCoCrCuNi-based equimolar high-entropy alloys. Mater. Sci. Eng. A **460**, 403–408 (2007)
45. A. Takeuchi, A. Inoue, Mixing enthalpy of liquid phase calculated by Miedema's scheme and approximated with sub-regular solution model for assessing forming ability of amorphous and glassy alloys. Intermetallics **18**(9), 1779–1789 (2010)
46. S.M. Oh, S.I. Hong, Microstructural stability and mechanical properties of equiatomic CoCrCuFeNi, CrCuFeMnNi, CoCrCuFeMn alloys. Mater. Chem. Phys. **210**, 120–125 (2018)
47. N. Derimow, T. Clark, C. Roach, S. Mathaudhu, R. Abbaschian, Processing pathway effects in CoCrCuNi + X (Fe, Mn) high-entropy alloys. Philos. Mag. **99**(15), 1899–1913 (2019)
48. B. Cantor, I. Chang, P. Knight, A. Vincent, Microstructural development in equiatomic multicomponent alloys. Mater. Sci. Eng. A **375**, 213–218 (2004)
49. F. Otto, A. Dlouhý, K.G. Pradeep, M. Kuběnová, D. Raabe, G. Eggeler, E.P. George, omposition of the single-phase high-entropy alloy CrMnFeCoNi after prolonged anneals at intermediate temperatures. Acta Mater. **112**, 40–52 (2016)
50. M.J. Aziz, Model for solute redistribution during rapid solidification. J. Appl. Phys. **53**(2), 1158–1168 (1982)
51. A.M. Mullis, R.F. Cochrane, Spontaneous grain refinement in alloy systems at low undercooling. Mater. Sci. Eng. A **304**, 267–271 (2001)
52. A. Singer, The physical chemistry of process metallurgy. Chem. Ind. **17**, 773–775 (1962)
53. K.I. Dragnevski, R.F. Cochrane, A.M. Mullis, The mechanism for spontaneous grain refinement in undercooled pure Cu melts. Mater. Sci. Eng. A **375**, 479–484 (2004)
54. R.F. Cochrane, S.E. Battersby, A.M. Mullis, The mechanisms for spontaneous grain refinement in undercooled Cu–O and Cu–Sn melts. Mater. Sci. Eng. A **304**, 262–266 (2001)

55. N. Haque, R.F. Cochrane, A.M. Mullis, The role of recrystallization in spontaneous grain refinement of rapidly solidified Ni3Ge. Metall. Mater. Trans. A **48**(11), 5424–5431 (2017)
56. E.G. Castle, A.M. Mullis, R.F. Cochrane, Evidence for an extensive, undercooling-mediated transition in growth orientation, and novel dendritic seaweed microstructures in Cu–8.9 wt% Ni. Acta Mater. **66**, 378–387 (2014)
57. A. Mullis, R. Cochrane, Grain refinement and the stability of dendrites growing into undercooled pure metals and alloys. J. Appl. Phys. **82**(8), 3783–3790 (1997)
58. A.F. Andreoli, X. Han, I. Kaban, In situ studies of non-equilibrium crystallization of AlxCoCrFeNi (x = 0.3, 1) high-entropy alloys. J. Alloys Compd. **922**, 166209 (2022)
59. J. Zhang, D. Hua, D. Cui, X. Li, K. Hua, Y. He, H. Wang, Y. Zhao, Subgrain-assisted spontaneous grain refinement in rapid solidification of undercooled melts. J. Mater. Sci. Technol. **174**, 234–248 (2024)
60. M. Schwarz, A. Karma, K. Eckler, D. Herlach, Physical mechanism of grain refinement in solidification of undercooled melts. Phys. Rev. Lett. **73**(10), 1380 (1994)
61. A. Karma, Model of grain refinement in solidification of undercooled melts. Int. J. Non-Equilib. Process. **11**(2), 201–233 (1998)
62. A.M. Mullis, The origins of spontaneous grain refinement in deeply undercooled metallic melts. Metals. **4**(2), 155–167 (2014)
63. S. Battersby, R. Cochrane, A. Mullis, Microstructural evolution and growth velocity-undercooling relationships in the systems Cu, Cu-O and Cu-Sn at high undercooling. J. Mater. Sci. **35**, 1365–1373 (2000)
64. D. Li, K. Eckler, D. Herlach, Undercooling, crystal growth and grain structure of levitation melted pure Ge and Ge-Sn alloys. Acta Mater. **44**(6), 2437–2443 (1996)
65. H. Zhang, W. Wu, Y. He, M. Li, S. Guo, Formation of core–shell structure in high entropy alloy coating by laser cladding. Appl. Surf. Sci. **363**, 543–547 (2016)
66. M. Robinson, D. Li, T. Rathz, G. Williams, Undercooling, liquid separation and solidification of Cu-Co alloys. J. Mater. Sci. **34**(15), 3747–3753 (1999)
67. W. Wang, Y. Wu, L. Li, W. Zhai, X. Zhang, B. Wei, Liquid-liquid phase separation of freely falling undercooled ternary Fe-Cu-Sn alloy. Sci. Rep. **5**, 16335 (2015)
68. D. Kashchiev, *Nucleation* (Elsevier, Amsterdam, 2000)
69. K.-Y. Tsai, M.-H. Tsai, J.-W. Yeh, Sluggish diffusion in Co–Cr–Fe–Mn–Ni high-entropy alloys. Acta Mater. **61**(13), 4887–4897 (2013)
70. G. Kurtuldu, P. Jarry, M. Rappaz, Influence of icosahedral short range order on diffusion in liquids: a study on Al-Zn-Cr alloys. Acta Mater. **115**, 423–433 (2016)
71. S.V. Divinski, A.V. Pokoev, N. Esakkiraja, A. Paul, A mystery of "sluggish diffusion" in high-entropy alloys: the truth or a myth? Diffus. Found. **17**, 69–104 (2018)

Publisher's Note Springer Nature remains neutral with regard to jurisdictional claims in published maps and institutional affiliations.